European Rotorcraft Forum

EXPERIMENTAL STUDY OF SECONDARY VORTEX STRUCTURES IN A ROTOR WAKE

C. Christian Wolf Clemens Schwarz Kurt Kaufmann Anthony D. Gardner
Institute of Aerodynamics and Flow Technology, German Aerospace Center (Germany)

Dirk Michaelis
LaVision GmbH (Germany)

Johannes Bosbach Daniel Schanz Andreas Schröder
Institute of Aerodynamics and Flow Technology, German Aerospace Center (Germany)

Abstract
The aerodynamic performance of a helicopter rotor is strongly affected by the structure of its wake. Rotor simulations using modern computational methods have the potential to capture high levels of detail, which recently triggered discussions of secondary vortex braids entangling the primary tip vortices. These structures are highly dependent on the numerical settings and need experimental validation. The current work investigates the wake of a subscale rotor in ground effect by time–resolved and volumetric flow field measurements using the "Shake–The–Box" technique. Both the Lagrangian tracks of the flow tracers and the derived gradient–based vortex criteria clearly verify the existence of secondary vortices. A post–processing scheme is applied to isolate these vortices in larger datasets. No distinct spatial organization of the structures was observed, but a slightly preferred sense of rotation which agrees to the shear of the wake swirl. The secondary structures were created shortly downstream of the rotor blades, starting at wake ages of about 70 degree.

Nomenclature

c	Chord length, $c = 0.061$ m
C_T	Thrust coeff., $C_T = T/(\rho(2\pi Rf)^2\pi R^2)$
f	Rotor frequency, $f = 20.83$ Hz
H	Rotor plane height, m
Q	Q–criterion, 1/s^2
Q_{neg}	Negative secondary vortex criterion, 1/s^2
Q_{pos}	Positive secondary vortex criterion, 1/s^2
Q_{tip}	Tip vortex criterion, 1/s^2
R	Rotor radius, $R = 0.775$ m
T	Rotor thrust, N
T_U	Turbulence level, see Eq. 1
u, v, w	Cartesian velocity components, m/s
V_h	Hover–induced velocity, $V_h = \sqrt{T/(2\rho\pi R^2)}$, m/s
V_{tip}	Blade tip velocity, $V_{\text{tip}} = 101.4$ m/s
x, y, z	Cartesian coordinate system, m
Δ	Difference between two values
ρ	Air density, $\rho = 1.18$ kg/m^3
Ψ	Azimuth angle, deg
Ψ_w	Tip vortex wake age, deg
$\vec{\omega}$	Vorticity vector, 1/s
∇	Nabla operator

Superscripts

$\overline{}$	Time–averaged value
$'$	Time–varying fluctuation value

Abbreviations

CFD	Computational fluid dynamics
DLR	German Aerospace Center
HFSB	Helium–filled soap bubbles
LED	Light–emitting diode
PIV	Particle image velocimetry
ppc	Particles per cell
STB	Shake-The-Box

1. Introduction

The wake of a helicopter main rotor is a highly three–dimensional and unsteady flow field. It is

characterized by the interaction of multiple structures such as the blade tip vortices, the blade shear layers, the rotor downwash, and the surrounding external flow. The wake has a strong influence on the aerodynamics of individual blades and on the performance of the entire rotor. Wake–related phenomena like blade–vortex interactions or the wake impingement on the tail boom are known to limit the flight envelope of a helicopter.

The capabilities of recent high–fidelity numerical simulations provide insight into the details of rotor wake aerodynamics. Figure 1 shows a result from Jain's[1] study of a hovering S-76 rotor, using a time–accurate OVERFLOW simulation with a high spatial resolution and SA–DES turbulence modeling in the wake region. The large–scale helical blade tip vortices are accompanied by many smaller–scaled structures. The detail at the bottom of Fig. 1 shows a series of secondary vortices which entangle two tip vortices. Similar phenomena were found in several other computational studies[2,3,4,5] and are subject to controversial discussions.

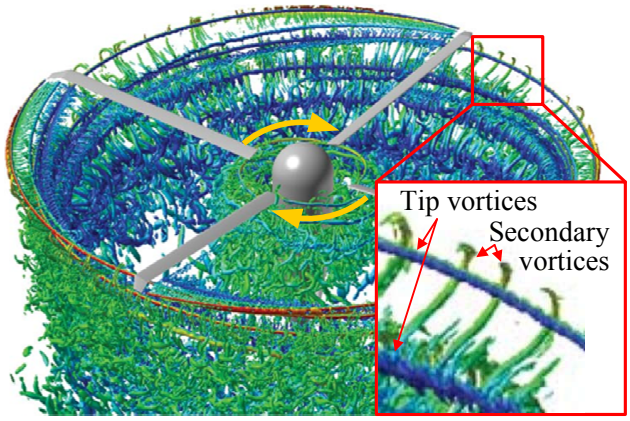

Figure 1: Four–bladed rotor wake visualized by isosurfaces of the Q–criterion, modified from Jain[1]

The wake layout of a two–bladed rotor is sketched in Fig. 2, with blue and red color marking the wakes of blade 1 and 2. The counterclockwise tip vortices convect along the slipstream boundary. The local downstream motion of the blade shear layers is driven by the spanwise lift distribution, and it is up to about twice as fast as the convection of the tip vortices. Therefore, the shear layers are only partly entrained by their corresponding tip vortex, and at some point they pass the preceding tip vortex. The outboard part of the shear layer is then stretched between the two tip vortices in an "S"–shaped layout, and a roll–up due to secondary instabilities is supposed to result in secondary vortex braids entangling the primary tip vortices.

Chaderjian and Buning[6] term the secondary vortices as "worms". They argue that their axial stretching in the velocity field of a pair of tip vortices augments the worms' rotation due to conservation of momentum. Hence, the worms are likely to occur in a phase where a blade shear layer approaches a preceding tip vortex. It is noted that the entire phenomenon has a strong resemblance to secondary vortex braids occurring in corotating Kelvin–Helmholtz instabilities of mixing layers (e.g. Bernal and Roshko[7]) or counterrotating von–Kármán vortices in the wake of bluff bodies (e.g. Gibeau et al.[8]).

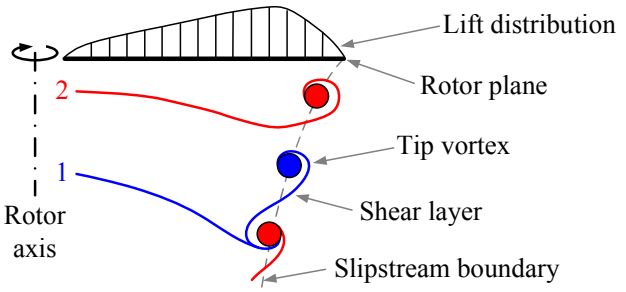

Figure 2: Schematic of a two–bladed rotor wake (blades 1/2), modified from Martin and Leishman[9]

Abras et al.[10] noted that the occurrence and structure of the secondary vortices in CFD rotor studies are largely dependent on the simulation time and on the numerical setup including mesh resolution or turbulence model. In some cases a breakdown of the entire wake due to secondary vortices was observed. The authors term this event "vortex soup" and discuss countermeasures applicable to the CFD setup. In a review of hover performance prediction workshops, Egolf et al.[11] list secondary vortex braids and their relation to the wake breakdown as an important unanswered question in modern rotor simulations, which underlines the need for experimental validation data.

The majority of wake–related rotor experiments studied pointwise or planar measurement regions, for example by applying flow visualization or particle image velocimetry to azimuthal slice planes[12] similar to the sketch in Fig. 2. In this case the secondary vortices leave footprints in the out–of–plane velocity, and several investigations found promising clues but no unambiguous proof. Therefore, a conclusive study of the complex spatial wake structure requires volumetric measurement techniques. The application of volumetric methods has gained increasing interest over the last decade despite the high experimental effort, as for example shown in a tip vortex study of a marine propeller using tomographic PIV[13].

The current work applies the time–resolved particle–tracking method "Shake–The–Box" (STB)[14] in combination with the data assimilation tool

"FlowFit"[15] to the rotor wake of a two–bladed subscale helicopter operated in ground effect. The measurement volume captures a part of the rotor wake's slipstream boundary, including several successive tip vortices, over an azimuthal segment of about $\Delta\Psi = 24°$. The results provide new insight into the flow structure and prove the existence of secondary vortex braids as predicted by CFD simulations.

2. Experimental setup

2.1. Model helicopter

The model helicopter "Align T-Rex 800" was rigidly mounted above a horizontal ground plate, see Fig. 3. The main rotor was equipped with two untwisted "Spinblades Black Belt 685" rotor blades, which had a radius of $R = 0.775\,\mathrm{m}$ and a chord length of $c = 0.061\,\mathrm{m}$. The distance between the ground plate and the rotor plane was set to either $0.7\,R$ or $1.0\,R$. The rotor speed was regulated, and monitored by a laser light barrier. The geometric blade pitch angle was adjusted through the collective swashplate setting. The thrust, T, was measured by a piezoelectric balance attached to the lower end of the model sting support.

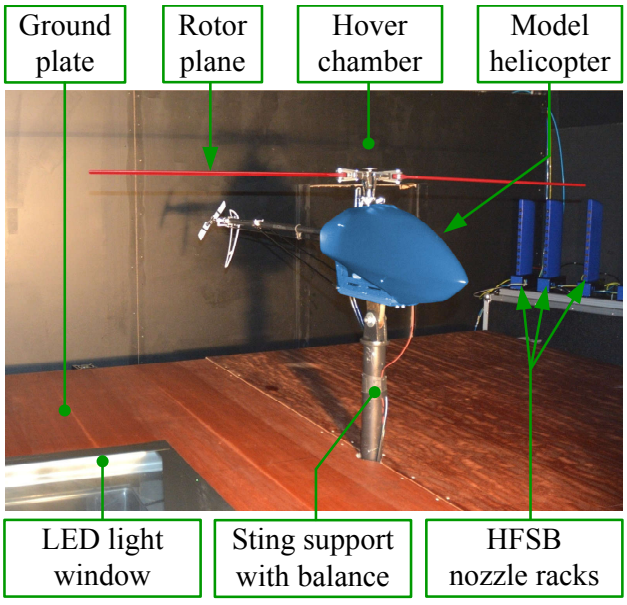

Figure 3: Model helicopter setup

2.2. Volumetric flow measurements

The volumetric flow fields were acquired using the STB method introduced by Schanz et al.[14]. The flow was seeded with helium–filled soap bubbles (HFSB) acting as tracer particles for the velocity of the surrounding fluid. The bubbles measured approximately $350\,\mu\mathrm{m}$ in diameter, and were generated through 130 HFSB nozzles with a design similar to that described by Bosbach et al.[16]. The nozzles were arranged in nine "linear nozzle arrays" and fed by two "LaVision HFSB" generators. About $6{\cdot}10^6$ neutrally buoyant HFSB per second were generated with the applied mass flow settings of the generators. The undisturbed lifetime of the bubbles amounts to about $100\,\mathrm{s}$ under laboratory conditions[17]. A homogeneous seeding density in the majority of the measurement domain was achieved shorty after rotor spin–up. However, distinct voids in the tip vortex centers were observed. The voids reveal limitations of the HFSB tracking fidelity, see section 3.2 for further discussions.

The output rate and lifetime of HFSB tracer bubbles is smaller than, for example, aerosolized oil droplets usually applied in particle image velocimetry. Therefore, an enclosed hover chamber of $7.2\,R \times 5.2\,R \times 5.2\,R$ with glass windows for optical access was designed to maintain a sufficient tracer seeding density in the rotor flow. A sketch of this setup is shown in Fig. 4.

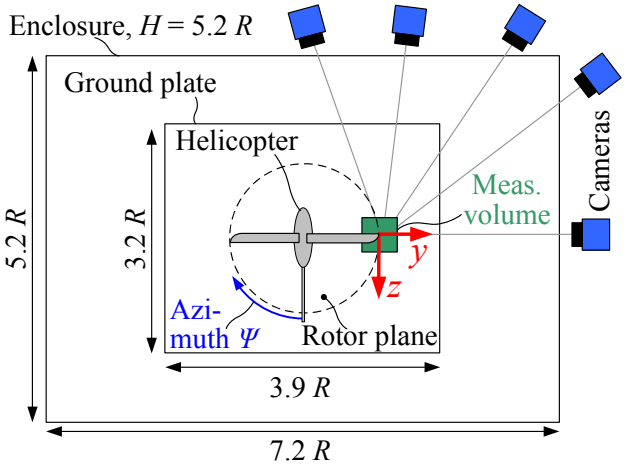

Figure 4: Sketch of the test section geometry

The measurement volume was illuminated using four high–intensity LED arrays "HardSoft ILM 501CG" with a total of 300 diodes. The green light pulses had a duration of $53\,\mu\mathrm{s}$ and a narrow beam angle, entering the test section through a flush–mounted glass insert in the ground plate. Figure 5 shows a long–term exposure of the experiment capturing multiple successive light flashes, indicating the particle tracks as pathlines.

A system of five high–speed cameras was installed, consisting of three "Phantom VEO 640L" and two "LaVision Imager HS 4M" cameras. The corresponding image sizes were set to 1600×2048 pixels and 1592×1776 pixels (width$\times$height) due to

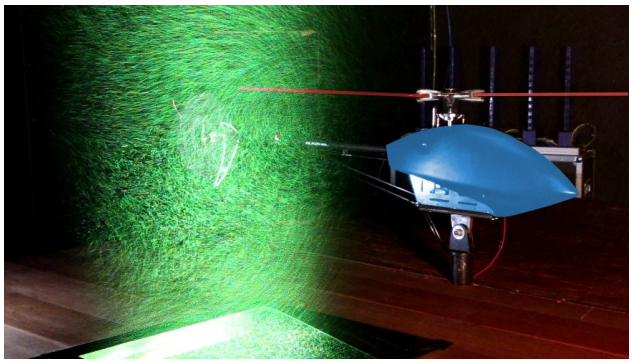

Figure 5: Illuminated STB measurement volume with HFSB tracer particles

bandwidth restrictions. All cameras were synchronized to the LED pulses and observed the volume from different viewing directions forming an included angle of slightly more than $90°$. The camera positions and tilt angles were adjusted so that the ground surface is at the image's lower edge and parallel to the viewing direction. This enables a tracking of soap bubbles close to the ground. The total number of bubbles within the measurement volume is larger than 10^5, and their image diameter ranged between three and five pixels, see Fig. 6.

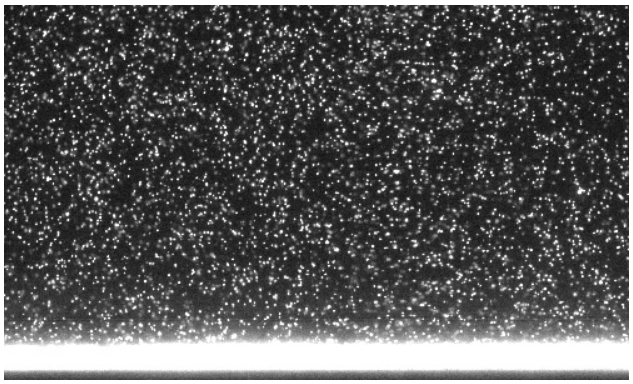

Figure 6: Cutout of a sample image showing HFSB bubbles and ground plate, 500×300 pixels

The camera viewing parameters were calibrated using a calibration target, which was imaged by all cameras simultaneously. Two parallel planes separated by $400\,\mathrm{mm}$ were recorded. The resulting calibrations were refined using volume self–calibration[18], and the volumetrically resolved particle imaging properties were extracted using a calibration of the optical transfer function[19].

The camera image repetition rate of $1.8\,\mathrm{kHz}$ ($\Delta t = 556\,\mu\mathrm{s}$) enabled a time–resolved Lagrangian particle tracking of the bubbles using the "Shake–The–Box" algorithm. This method exploits the time information and converges to a state where nearly all imaged particles are tracked. In a first processing pass the number of tracked particles increases from about $5 \cdot 10^4$ to 10^5 over the first 50 time steps. A second pass, working on a time–reversed image sequence and extending the known tracks backwards in time, further increases the number of tracked particles. The tracks are post–processed using the B–spline based filtering approach "TrackFit"[15] with a smoothing parameter, the crossover frequency, set to 0.2. The resulting position accuracy is estimated to $38\,\mu\mathrm{m}$.

In a second step, the flow field in the full measurement volume is interpolated using DLR's "FlowFit"[15] approach, which is based on a data assimilation scheme using cubic spline functions resulting in a continuous representation of the time-resolved 3D velocity and pressure fields. The evaluation was then restricted to a rectangular region of interest covering $585\,\mathrm{mm}$ ($0.75\ R$) in height and $385\,\mathrm{mm}$ ($0.5\ R$) in both width and depth. For the current test cases this volume contains $8.3 \cdot 10^4 \pm 12\%$ valid particles depending on the time–varying seeding density. FlowFit's spline system was set to a cell spacing of $4\,\mathrm{mm}$ ($5.2 \cdot 10^{-3}\ R$) corresponding to an average ratio of 0.06 particles per cell (ppc), which is similar compared to preceding studies with about 0.1 ppc[17,20]. In a non-linear optimization scheme FlowFit minimizes cost functions for the differences of velocity and acceleration at the Lagrangian particle tracks while continuity and conservation of momentum is enforced in the full volume. The resulting Eulerian flow description is then calculated by sampling the spline functions to a regular Cartesian grid with a spacing of $2\,\mathrm{mm}$ ($2.6 \cdot 10^{-3}\ R$). The volumetric data can now be used to calculate vortex identification criteria based on the local velocity gradients.

For each test condition a total of 3800 flow fields, corresponding to about 44 rotor revolutions, were acquired to enable statistical analyses.

3. Results and discussion

3.1. Test cases and average flow field

The experiments were conducted at a constant rotor frequency of $f = 20.83\,\mathrm{Hz}$, corresponding to a tip speed of $V_{\mathrm{tip}} = 101.4\,\mathrm{m/s}$. The test cases "TC1" and "TC2" use the same collective swashplate setting with a geometric blade pitch angle of about $10°$, but different rotor heights above ground ($H/R = 0.7$ versus $H/R = 1.0$). The lower height results in a slightly higher thrust ($T = 108\,\mathrm{N}$ versus $T = 99\,\mathrm{N}$) due to the increased ground effect. The settings correspond to about 80% of the rotor's maximum thrust setting, and a thrust–to–weight ratio of about two considering the free–flying model helicopter. Table 1 summarizes the relevant aerodynamic

parameters of both cases. The hover–induced velocity V_h calculated from the momentum theory is used as a reference value for the measured wake velocities.

	TC1	TC2
Rotor frequency f, Hz	20.83	
Rotor height H/R	0.7	1.0
Thrust, N	108	99
Thrust coefficient C_T	0.0047	0.0043
Hover–ind. velocity V_h, m/s	4.93	4.70

Table 1: Conditions for test cases 1 and 2

Figure 7 shows the time–averaged flow field for TC1, with the grid borders corresponding to the size of the STB volume. The x–axis is collinear to the rotor axis and points downwards. The y–axis coincides with the azimuth angle $\Psi = 270°$, that is, the blade's spanwise direction when it points to the right (also see Fig. 4). The z–axis points in the direction of the blade motion. The coordinate origin was set to the blade tip position determined by the camera system. The tip–to–ground distance was therefore slightly larger (up to 20 mm or 0.03 R) than the nominal rotor disk height in Tab. 1 due to the bending of the rotating blade under airloads. The red line in Fig. 7 marks the tip's path in the STB volume.

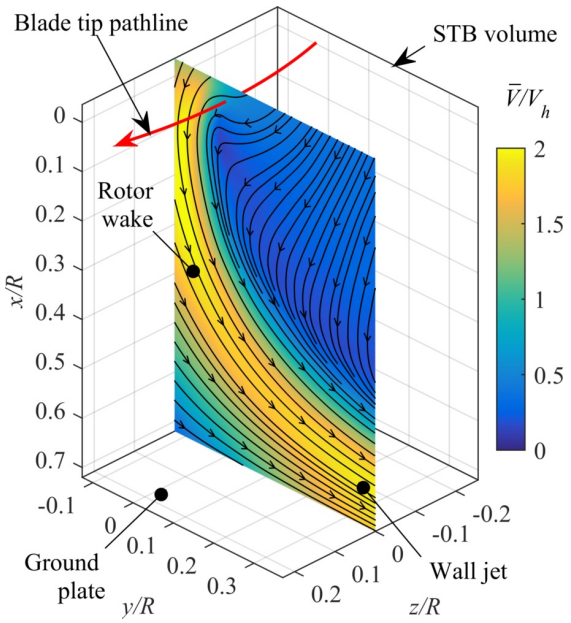

Figure 7: TC1, measurement volume and time–averaged flow field

The velocity levels and the streamline pattern of the $z = 0$–slice plane in Fig. 7 show large parts of the rotor wake's slipstream boundary. The downwash velocity magnitude $\overline{V}$ reaches its maximum of about twice the hover–induced velocity V_h at a radial position of 0.1 R inboard of the tip. Shortly below the rotor plane the wake contracts towards the rotor axis in the negative y–direction, before being deflected outboard and forming a wall jet due to the proximity of the ground plate. The entrainment of external flow can also be seen, particularly by means of the inboard–directed, almost horizontal streamlines in the blade tip region.

Figure 8 compares the flow patterns of TC1 (left, repeated from Fig. 7) and TC2 (right). For TC2 the position of the STB volume was kept constant but the height of the rotor plane H/R was increased by 0.3, meaning that the early wake development is no longer captured. The larger ground clearance results in a smaller curvature of the wake boundary, and the wall jet at the right border of the volume is slower and further away from the ground.

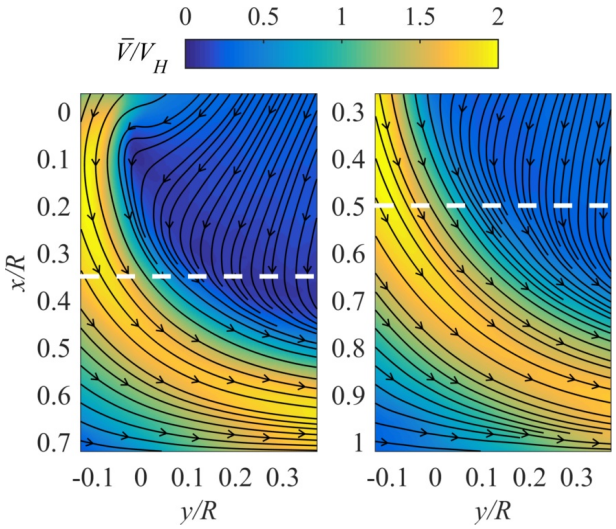

Figure 8: TC1 (left) and TC2 (right), time–averaged flow field at $z = 0$

The black lines in Fig. 9 are the time–averaged normalized velocity profiles extracted halfway between rotor plane and ground level, at $x/R = 0.35$ for TC1 and $x/R = 0.50$ for TC2 as indicated by white dashed lines in Fig. 8. At this stage the average wake profile of both test cases is very similar. The velocity fluctuation level can be expressed by the overall turbulence level T_U,

$$T_U = \frac{1}{V_h}\sqrt{\frac{1}{3}\left(\overline{u'^2} + \overline{v'^2} + \overline{w'^2}\right)}, \quad (1)$$

as indicated by red lines in Fig. 9. The highest levels of up to 50% are found in the wake's shear layer at $y = 0$, they coincide with the steepest velocity gradient $\partial\overline{V}/\partial y$.

A decomposition into Cartesian velocities shows that the time–averaged wake contains a positive w–component pointing in rotor–tangential direction.

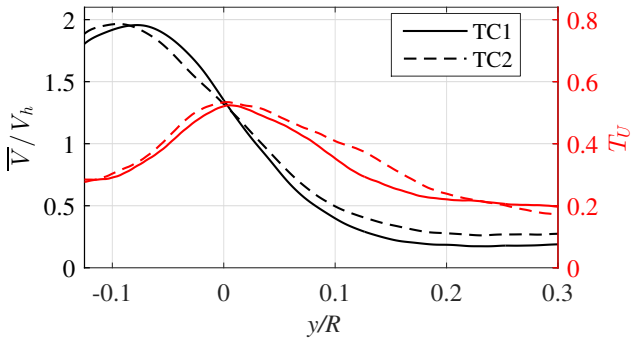

Figure 9: Average velocity and turbulence level at $z=0$ and $x/R=0.35$ (TC1) or $x/R=0.50$ (TC2)

This component represents the wake swirl due to the rotation of the blades, see the blue line and red arrow markers in Fig. 10 (top). The swirl velocity level is up to $20\%\ V_h$ or $1\,\mathrm{m/s}$. The resulting radial gradient $\partial\overline{w}/\partial y < 0$ towards the external flow could be the source of an asymmetric secondary vortex creation in the slipstream boundary, see section 3.4.

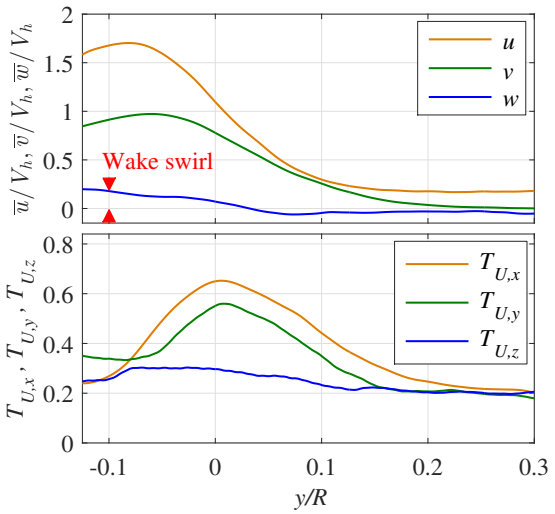

Figure 10: Velocity components (top) and turbulence levels (bottom) in x, y, z–direction at $z=0$ and $x/R=0.35$ (TC1)

When considering the components of the turbulence level in Fig. 10 (bottom), for example in x–direction defined as

$$T_{U,x} = \frac{1}{V_h}\sqrt{\overline{u'^2}}, \tag{2}$$

it can be seen that the velocity fluctuations are strongly anisotropic. The overall T_U–peak at $y=0$ is reflected by the $T_{U,x}$– and $T_{U,y}$–components (green and orange lines) with maximum values around 60%, whereas the $T_{U,z}$–component (blue line) exhibits only slightly increased levels of about 30% throughout the entire shear layer region between $-0.1 < y/R < 0.15$. This anisotropy indicates large–scale coherent flow structures, in particular the tip vortices, which induce x, y–velocity fluctuations due to their spatial alignment. In the external flow, $y/R > 0.2$, all three T_U–components agree on a common isotropic level around 20%.

3.2. Vortex identification and particle tracks

Figure 11 shows the instantaneous vortical structure of a sample flow field taken from test case TC1. The green isosurfaces correspond to a positive threshold for the Q–criterion as calculated from the three–dimensional velocity gradient tensor.

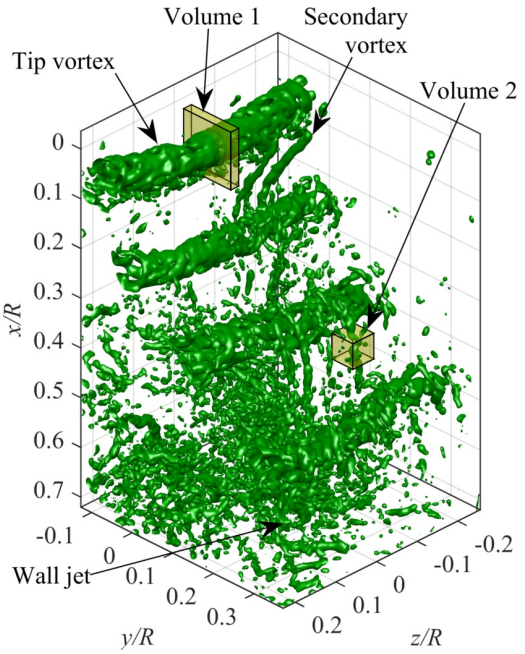

Figure 11: TC1, instantaneous Q–isosurfaces

Four blade tip vortices appear as cylindrical structures aligned in the z–direction. They were created during two revolutions of the two–bladed rotor and have wake ages of $\Psi_w = 70°, 250°, 430°$, and $610°$ at $z = 0$. The vortices convect downstream along the slipstream boundary, and they become increasingly disorganized with advancing wake age. Some secondary vortices stretch between the primary tip vortices, but they are masked by measurement noise and small–scale aerodynamic turbulence which cannot be properly resolved with the current mean distance of tracer particles. Particularly the wall jet close to the ground surface appears as a chaotic and unordered region of high turbulence. Further post–processing is required to isolate the relevant structures. This will be illustrated with reference to two sub–volumes marked by

yellow boxes in Fig. 11, containing a primary vortex (volume 1) and a secondary vortex (volume 2).

A left side view of the velocity field in volume 1 as predicted by FlowFit showing every third velocity vector in both x, y–directions is in Fig. 12a. It is dominated by the circulation of the tip vortex, which is apparent when subtracting the central convection velocity (red arrow) yielding the velocity vectors in the tip vortex reference frame (black arrows).

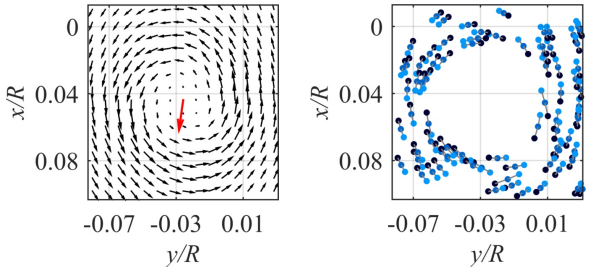

(a) Velocity vectors (→) after subtracting the vortex convection (→)

(b) Convection–corrected particle tracks, positions at $t-\Delta t$, t, $t+\Delta t$ (•, •, •)

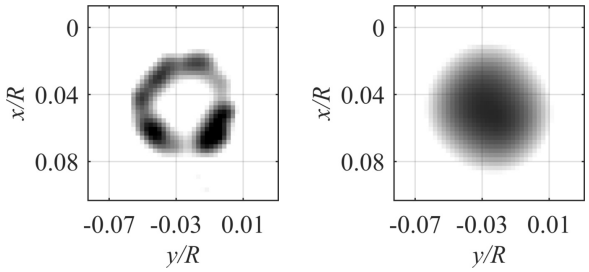

(c) Decomposed unfiltered Q_{tip}–criterion

(d) Decomposed filtered Q_{tip}–criterion

Figure 12: Tip vortex in volume 1 of Fig. 11, left side view

The volume contains 78 tracer particles, whose convection–corrected tracks for three successive acquisition time steps ($t-\Delta t, t, t+\Delta t$) are shown in Fig. 12b. All tracks agree on a counterclockwise rotational motion around a common center, but the center itself contains a particle void indicating deficiencies in the flow–tracing ability of the soap bubbles. The velocity information within the vortex core is therefore unreliable, and the current work will not discuss tip vortex–core related properties such as core radius or maximum swirl velocity. It is noted that Caridi et al.[21] achieved a sufficient HFSB seeding of a delta–wing leading–edge vortex. However, the vortex creation differs from the current case, given that Caridi's wing has a smaller inflow velocity and a much larger effective chord length along which the vortex is created. History– and particle size–effects may play a crucial role, and even a slight density mismatch to the surrounding fluid has a large impact under the strong centrifugal forces.

The scalar Q–value is decomposed into Cartesian components as proposed by Gibeau et al.[8] using the vorticity unit vector $\vec{\omega}_n$, that is, the direction of the vorticity:

$$(3) \quad \vec{\omega}_n = \begin{pmatrix} \omega_{n,x} \\ \omega_{n,y} \\ \omega_{n,z} \end{pmatrix} = \frac{\nabla \times \vec{u}}{|\nabla \times \vec{u}|}$$

Other approaches to directional vortex criteria, such as the "Rortex"–criterion defined by Gao and Liu[22], do not change the findings of this study. The tip vortices can now be identified using

$$(4) \quad Q_{\text{tip}} = \begin{cases} -\omega_{n,z} \cdot Q; & \omega_{n,z} < 0 \\ 0; & \omega_{n,z} \geq 0 \end{cases} .$$

The negative sign is introduced so that the tip vortices have positive Q_{tip}–values despite their negative z–rotational sense. A transformation into rotor hub–centered cylinder coordinates is disregarded, since the volume only covers an azimuthal range of $\Delta\Psi = \pm 12°$, and the related curvature of the vortex tubes is small. The Q_{tip}–distribution for volume 1 is given in Fig. 12c, representing a slice cut through the tip vortex. The highest values are observed in an annular region close to the innermost tracer particles. This annular shape is due to the invalid velocity information within the particle void, since the peak Q–values are always expected in the center of a vortex. Therefore, a convolution filter is applied in order to correctly capture the shape and the central position of the tip vortices. This method was proposed by van der Wall and Richard[23] with a view to tracer voids, and later applied by Bauknecht et al.[24]. The current filter kernel for Q_{tip} uses a Gauss distribution adapted to an expected radius of 24 mm $(3.1\,\%\,R)$. The convolution–filtered result, see Fig. 12d, fills the void without altering the shape of the unfiltered Q_{tip}–distribution.

A top–down view of the secondary vortex flow in volume 2 is given in Fig. 13a, here showing every second velocity vector in both y/z–directions. The central convection velocity (red arrow) is larger than the swirl velocities of the vortex itself, but a subtraction still reveals the circular flow pattern. The secondary vortex's sphere of influence is small in comparison to the tip vortex. A saddle point is created in the flow (orange diamond marker), and the vectors in the upper right corner of Fig. 13a do not comply with the swirling motion.

Volume 2 contains 58 tracer particles, whose tracks are shown in Fig. 13b. There is no distinct particle void in which the tracer density is significantly lower than in the rest of the volume. The majority of the tracer bubbles, except for those in the upper

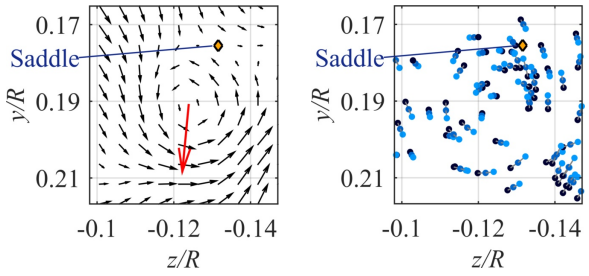

(a) Velocity vectors (→) after subtracting the vortex convection (→)

(b) Convection–corrected particle tracks, positions at $t-\Delta t$, t, $t+\Delta t$ (•, •, •)

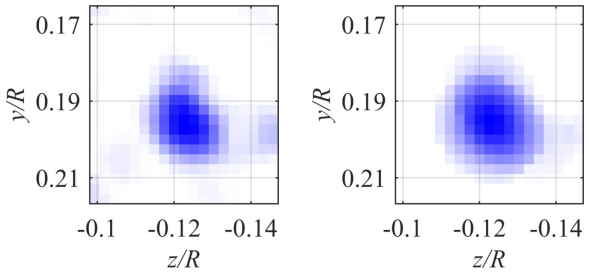

(c) Decomposed unfiltered Q_{neg}–criterion

(d) Decomposed filtered Q_{neg}–criterion

Figure 13: Secondary vortex in volume 2 of Fig. 11, top–down view

right corner, have a coherent counterclockwise motion around a common center. This means that the secondary vortex can be identified from the time–resolved tracer particle position data, without FlowFit or vortex identification criteria, which is an important proof for the existence of these vortices.

The chosen criterion for secondary vortices multiplies the Q–values with a projection of the unit vorticity vector onto the x, y–plane,

$$\omega_{n,xy} = \sqrt{{\omega_{n,x}}^2 + {\omega_{n,y}}^2}\,, \tag{5}$$

to account for the oblique S–shape of the structures. The positive and negative senses of rotation are determined by the sign of the $\omega_{n,x}$–component:

$$Q_{\text{pos}} = \begin{cases} \omega_{n,xy} \cdot Q; & \omega_{n,x} > 0 \\ 0; & \omega_{n,x} \leq 0 \end{cases} \tag{6}$$

$$Q_{\text{neg}} = \begin{cases} \omega_{n,xy} \cdot Q; & \omega_{n,x} < 0 \\ 0; & \omega_{n,x} \geq 0\,. \end{cases} \tag{7}$$

The rotational motion in Figs. 13a and 13b points in the negative x–direction and is therefore captured by the Q_{neg}–criterion as shown by the blue coloring in Fig. 13c. The secondary vortex can be clearly identified without further postprocessing. Nevertheless, a convolution filter is applied to be consistent with the tip vortex–procedure and to remove residual small–scale structures. The filter size was adapted to a smaller core size, assuming a filter radius of 8 mm or 1% R. This corresponds to one third of the tip vortex diameter, and the result of this filter is given in Fig. 13d.

As a last filter step, only coherent volumes exceeding a threshold for Q_{tip}, Q_{pos}, or Q_{neg} are accepted. The secondary structures are expected to

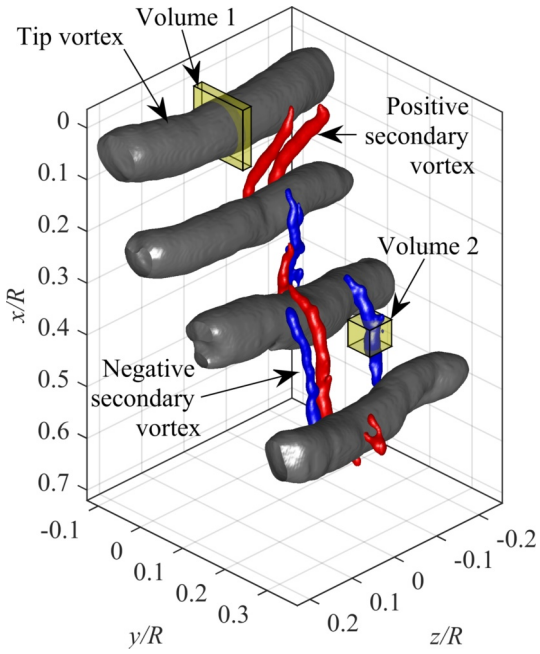

Figure 14: TC1, instantaneous isosurfaces of the decomposed criteria Q_{tip}(•), Q_{pos}(•), and Q_{neg}(•)

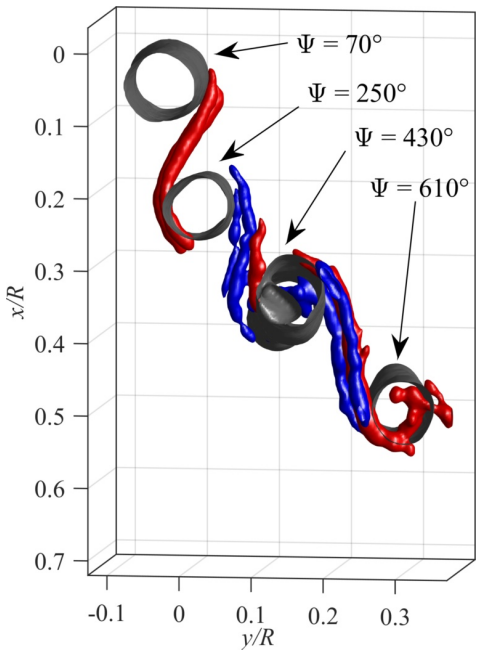

Figure 15: TC1, left side view of Fig. 14

be slender, inducing an additional geometric aspect ratio–constraint with a minimum height of $\Delta x/R = 0.15$ at a maximum width of $\Delta z/R = 0.08$. The result of this post–processing scheme applied to the entire STB volume is shown in Fig. 14.

In contrast to Fig. 11, the flow structure can now be clearly identified. The earliest secondary structures are created at a young wake age, here stretching between the first two tip vortices aged about $\Psi_w = 70°$ and $\Psi_w = 150°$. In this example both positive and negative senses of rotation, corresponding to red and blue isosurfaces, occur simultaneously and in roughly equal shares. A more detailed statistical analysis of the entire dataset is in section 3.4.

The interaction between primary and secondary structures is visualized in a left side view of the measurement volume, see Fig. 15. The secondary structures stretch between the tip vortices on an S–shaped path, which supports the findings of earlier computational studies as discussed in Fig. 1, and the close relation between secondary vortices and blade shear layer as discussed in Fig. 2.

3.3. Aperiodicity and tip vortex trajectories

The structure of four additional TC1 flow samples is shown in Fig. 16. The rotor azimuth and, hence, the age of the tip vortices are the same as in Fig. 14.

The vortex identification scheme is universally applicable, but the occurrence, position, and inclination of the secondary vortices are different in individual rotor revolutions. From a visual inspection of the entire TC1 data no recurring spatial organization of the secondary structures, for example in terms of a regular spacing distance or alternating senses of rotation, was observed. The existence of an ordered structure is implied by other secondary–instability phenomena, for example found in the wake of a bluff body[8]. However, most of the corresponding studies were conducted at much lower Reynolds numbers and smaller flow aperiodicities.

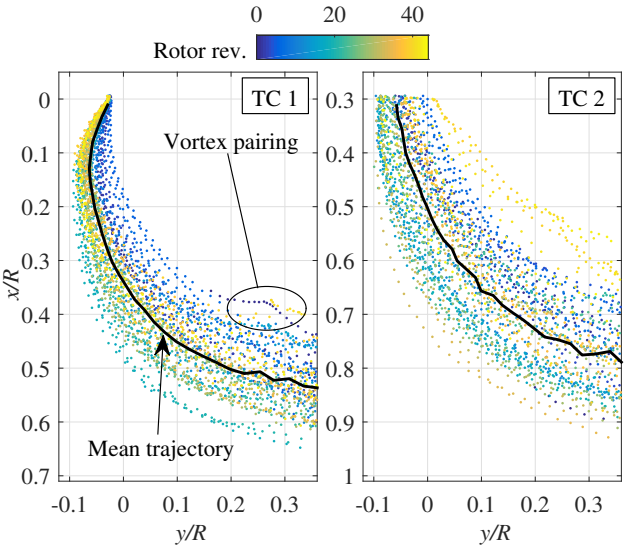

Figure 17: TC1 (left) and TC2 (right), identified tip vortex centers and mean trajectory

A common way to gain a deeper insight into the data is to analyze the phase–averaged wake properties as a function of its age Ψ_w, probably using additional conditions such as outlier removal, modal filtering, etc. This approach is hampered in the current case since even the primary vortices have a pronounced aperiodicity. The tip vortex center positions were identified in the $z = 0$–plane over the entire TC1 and TC2 measurement intervals of $\Delta t = 2.1$ s, or about 44 rotor revolutions. The centers are shown in Fig. 17 for every fifth time step. Due to the different rotor heights in relation to the fixed STB volume, the tip vortices can be tracked with a minimum age of $\Psi_w \approx 0°$ for TC1 (shortly behind the blade's trailing edge), and $\Psi_w \approx 340°$ for TC2.

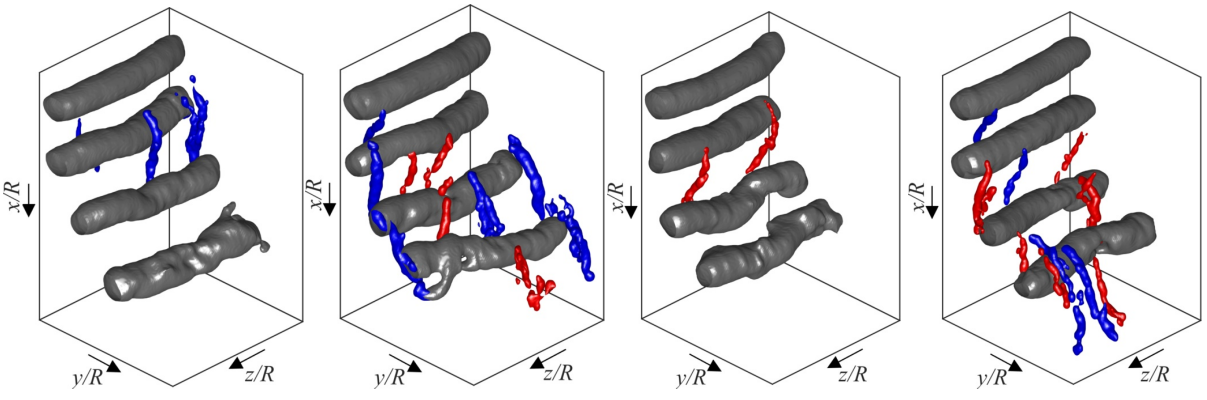

Figure 16: TC1, instantaneous samples, wake age and visualization of Q_{tip}(•), Q_{pos}(•), Q_{neg}(•) as in Figs. 14, 15

A significant scatter of the individual tip vortex trajectories is apparent, which increases from younger to older wake ages. When leaving the measurement volume in the lower right corners the mean trajectories (black lines) are located $0.18\ R$ (TC1) and $0.21\ R$ (TC2) above ground, but the individual positions scatter with a standard deviation of about $0.05\ R$ (TC1) or $0.08\ R$ (TC2). No systematic difference between both rotor blades was found. The vortex trajectories and the wake boundary are slowly altered over the course of several rotor revolutions, which can be seen from the color–coded time stamps of the data points. A pronounced unsteadiness of the vortex trajectories in ground effect has been reported for both model scale[25,26] and full scale[27,28] tests. In the current case it is suspected that the unsteadiness is further promoted by the confined test stand enclosure.

Some of the trajectories have distinct bumps, which are connected to the "vortex pairing" phenomenon. This long–wave instability mechanism[29] does not depend on secondary structures but can be caused by an uneven spacing of primary vortices inducing a pairwise orbital motion around each other. Pairing phenomena are frequently reported in rotor wake studies, particular in the presence of ground effects[28,30] promoting large–scale unsteadiness. A prominent pairing–related upward deflection of a TC1 vortex trajectory is highlighted in Fig. 17, left. The corresponding volumetric process is shown Fig. 18 by means of four consecutive Q_{tip}–visualizations with a wake age stepping of $\Delta\Psi_w = 70°$. In Fig. 18a vortex A has an age of about $\Psi_w = 570°$, and the separation distance to the successive vortex B is notably smaller than usual. After the separation distance is further decreased and the vortex tubes A and B are bent towards each other (Fig. 18b), the mutually induced velocity fields decelerate and raise vortex A but accelerate and push down vortex B (Fig. 18c). This initiates the orbital motion and the corresponding deflections of the trajectories. As a result, vortex B overtakes vortex A and the order is reversed (Fig. 18d) shortly before both structures leave the measurement volume. In some other cases the pairing was even followed by a merging of tip vortices. Regarding the entire test interval of TC1, an irregular pairing structure of older tip vortices with $\Psi_w > 360°$ was

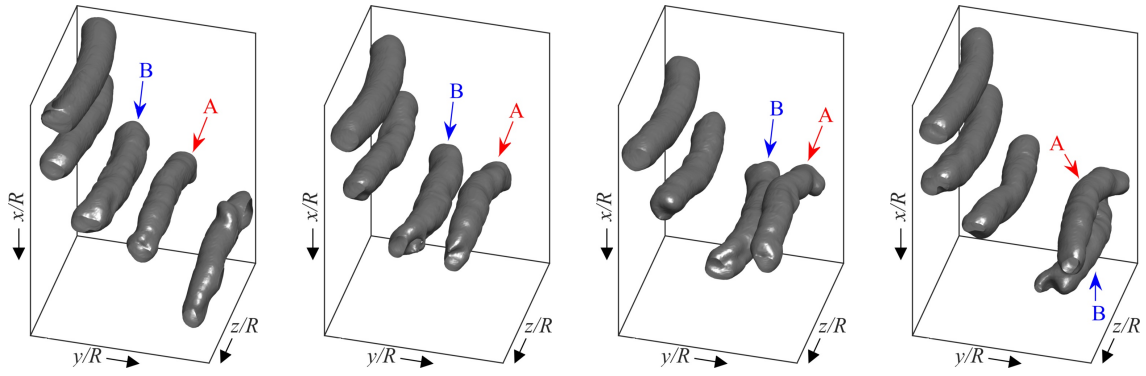

(a) Vortex A: Ψ_w = 570° (b) $\Psi_w + 70°$ (c) $\Psi_w + 140°$ (d) $\Psi_w + 210°$

Figure 18: TC1, Paring process of tip vortices A and B visualized by Q_{tip}(•)

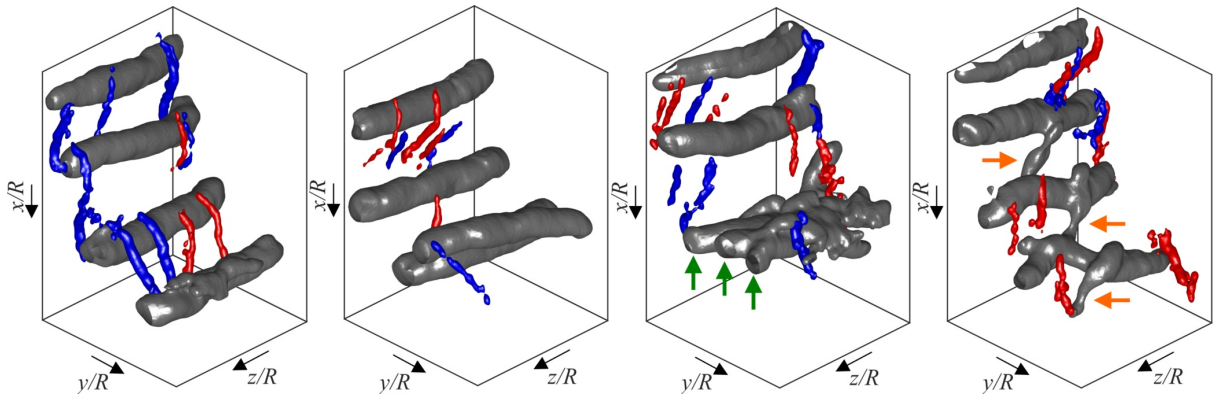

(a) (b) (c) (d)

Figure 19: TC2, instantaneous samples, visualization of Q_{tip}(•), Q_{pos}(•), Q_{neg}(•) as in Figs. 14, 15

observed in about one third of the rotor revolutions.

Figure 19 shows four instantaneous flow fields from TC2, and the general findings are similar to TC1 despite the rotor's larger ground clearance and the higher wake age in the STB volume. There are samples with regularly spaced tip vortex tubes entangled by secondary structures (Fig. 19a) as well as pairing events with a reversed tip vortex order (Fig. 19b). In some few examples an even more complicated breakdown of the primary vortex system was observed at older wake ages. This includes the pairing and merging process of three tip vortices, see the green arrow markers in Fig. 19c. Figure 19d shows an instantaneous flow field in which a series of three secondary structures (see the orange arrow markers) are tightly coupled to the tip vortices and tilted in the z–direction, therefore, the entire structure is identified as a single coherent vortex volume appearing in gray color. The centerlines of the tip vortices are strongly distorted, resulting in a "criss–cross" vortex pattern which successively breaks down into smaller structures. Complex three-dimensional breakdown mechanisms involving secondary vortices have been described before, for example regarding the interaction of two collinear and corotating vortex tubes, see Leweke et al.[31] for a comprehensive review.

3.4. Time– and phase–averaged statistics

The time–averaged secondary vortex strengths Q_{pos} and Q_{neg} were calculated over 3800 flow samples, differentiating between positive and negative senses of rotation. The results for TC1, see Fig. 20a, and TC2, see Fig. 20b, were additionally averaged in the z–direction over the STB volume's entire width. The quantitative levels of Q_{pos} and Q_{neg} are not interpreted, but all figures use the same isoline values to enable a direct comparison.

The distribution of secondary Q–values closely follows the rotor wake boundary and the mean trajectories of the tip vortices (black lines). In streamwise direction the largest values of both test cases and both senses of rotation are observed between about $0.3\,R$ and $0.5\,R$ below the rotor plane, corresponding to tip vortex ages Ψ_w between $340°$ and $600°$. This also implies a secondary vortex formation for $\Psi_w < 340°$ and a vortex dissolution for $\Psi_w > 600°$.

An overall comparison of Q_{pos} (red coloring) and Q_{neg} (blue coloring) reveals larger Q_{neg}–values in both test cases, that is, a slight preference towards a negative sense of rotation. The rotational direction of the blades can be the cause for this imbalance. As already shown by the blue line in Fig. 10 (top), the wake's swirl results in a positive rotor–tangential

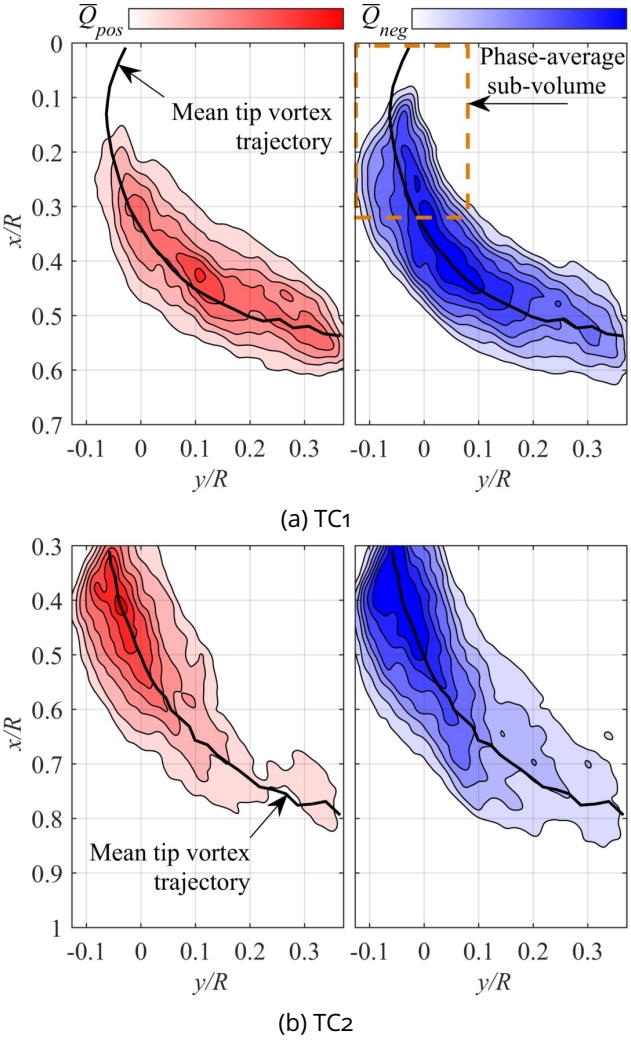

Figure 20: Time–averaged secondary vortex strength Q_{pos} (left, •) and Q_{neg} (right, •)

$\overline{w}$–velocity component. The shear in the slipstream boundary, $\partial\overline{w}/\partial y < 0$, coincides with a negative rotational sense of the secondary vortices. However, experimental asymmetries such as the helicopter's tail boom or the rectangular ground plate and test enclosure, or slightly de–trimmed rotor blades may also be the cause.

The aperiodicity of the flow as discussed in section 3.3 impedes the interpretation of phase–averaged quantities. On the background of the tip vortex scatter and the time–averaged Q_{pos}– and Q_{neg}–distributions, the most promising approach is to investigate negative secondary vortices in the early rotor wake of TC1. A corresponding sub–volume was selected, as sketched by the dashed orange line in Fig. 20a (right). In each instantaneous measurement the rotor azimuth angle Ψ was used to calculate the local age of the youngest tip vortex Ψ_w in planar slices of the volume at constant z–levels. The wake is periodic with a length of

$\Delta\Psi_w = 180°$ when assuming that the aerodynamics of the two rotor blades are identical. The Q–distributions of the slices were binned according to Ψ_w in intervals of $10°$ and then phase–averaged. Figure 21 shows a subset of the results for eight different tip vortex ages.

The gray circular areas represent high values of Q_{tip} and, therefore, the approximate phase–averaged position of the primary tip vortices. The tip vortex downward motion along the slipstream boundary is clearly visible. The marked gray areas are larger than the individual vortices due to the aperiodic scatter eroding the phase statistics. For single vortices, this aperiodicity can be countered by identifying and aligning the individual vortex center positions, for example shown by Kindler et al.[32]. However, this approach is not useful in the current situation when treating a system of multiple interleaving primary and secondary structures.

Shortly downstream of the rotor blades, at an age of $\Psi_w = 0° \ldots 10°$ shown in Fig. 21a, the youngest tip vortex is located near the top of the measurement region. Its center is slightly above ($x < 0$) and inboard ($y < 0$) of the tip position due to the roll–up process over the suction side of the blade tip. Note that there are no significant secondary Q–values in between the first two tip vortices, which is expected since the youngest trailing blade shear layer is still close to its corresponding primary vortex. Further downstream large Q_{neg}–values, represented by blue coloring, entangle the older tip vortices aged $180° \ldots 190°$ and $360° \ldots 370°$. Figures 21b and 21c show that there are no significant changes in the wake structure up to a vortex age of about $\Psi_w = 70°$, apart from the downward convection motion. Structured secondary vortices leave a footprint in the phase–averaged statistics starting at about $\Psi_w = 70°$, see Fig. 21d. This phase corresponds to secondary structures observed in instantaneous volumetric Q–distributions discussed in sections 3.2 and 3.3, for example see Figs. 14, 16a, or 16d with $\Psi_w = 70°$ at $z = 0$. The statistics reveal a further increase in phase–averaged secondary vortex strength Q_{neg}, see Figs. 21e and 21f, before reaching the fully developed "S"–shaped layout at about $\Psi_w = 110° \ldots 120°$. It is known from the

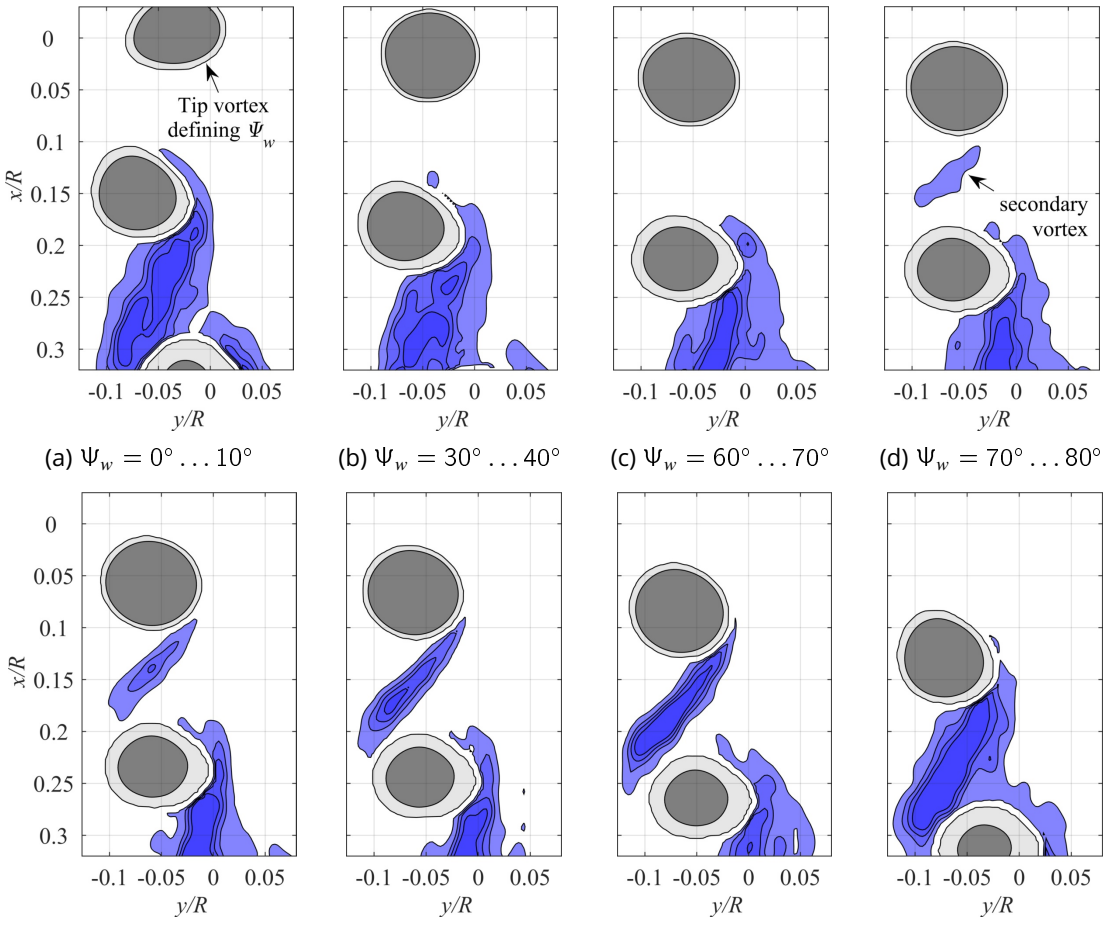

(a) $\Psi_w = 0° \ldots 10°$ (b) $\Psi_w = 30° \ldots 40°$ (c) $\Psi_w = 60° \ldots 70°$ (d) $\Psi_w = 70° \ldots 80°$

(e) $\Psi_w = 80° \ldots 90°$ (f) $\Psi_w = 90° \ldots 100°$ (g) $\Psi_w = 110° \ldots 120°$ (h) $\Psi_w = 160° \ldots 170°$

Figure 21: Phase–averaged tip vortex strength Q_{tip} (•) and negative secondary vortex strength Q_{neg} (•)

instantaneous samples that the occurrence of secondary structures persists until much older wake ages, but the layout of the phase–averaged structures is increasingly blurred and eroded due to the increasing aperiodic wake scatter, for example see Fig. 21h for $\Psi_w = 160° \ldots 170°$.

4. Conclusions

The major results of this study can be summarized as follows:

- Shake–The–Box Lagrangian particle tracking with subsequent regularized interpolation using FlowFit was successfully applied to measure volumetric and time–resolved flow fields in the wake of a subscale helicopter main rotor. The data provides insight into the three–dimensional wake structure which cannot be acquired by the usual planar measurement regions.
- The existence of secondary vortex structures was verified by both Lagrangian tracks of the HFSB flow tracers and the derived vortex identification criteria. To the authors' knowledge this is the first conclusive experimental proof. The secondary braids entangle the primary tip vortices in an "S"–shaped layout and originate in the blade's shear layer. A data post–processing routine based on spatial filters and a decomposition of the Q–criterion was applied to isolate the wake's vortical structure in large datasets.
- The rotor was operated in ground effect, resulting in a high wake unsteadiness and a large aperiodicity of the primary blade tip vortices, which were partly involved in vortex pairing processes.
- The secondary vortices showed no distinct spatial organization such as a preferred separation distance or an alternating sense of rotation. The existence of such an organization is implied by other secondary instability phenomena, but may be covered by the turbulence and aperiodicity of the chosen test case. However, a slight preference towards a (in the current definition) negative sense of rotation was found. This sense complies with the shear stresses induced by the wake's swirl, which originates in the blade rotation direction.
- Both instantaneous and phase–averaged results showed that the secondary structures are created at an early wake age, starting at an azimuth angle of about $70°$ in the rotor plane and downstream of each blade. This result corresponds to numerical simulations. It confirms the hypothesis that the secondary vortices are augmented by the stretching of a blade shear layer under the influence of the tip vortex of the preceding rotor blade.

5. Acknowledgments

The studies were conducted as a part of the DLR project "FAST-Rescue". The authors thank Markus Krebs, Janos Agocs, Andreas Goerttler, Felix Wienke, and Uwe Dierksheide for their support during the measurements.

References

[1] Jain, R.: "Sensitivity Study of High–Fidelity Hover Predictions on the Sikorsky S-76 Rotor", *Journal of Aircraft* **55** (1), 2018, pp. 78–88. doi: 10.2514/1.C034076.

[2] Chaderjian, N. M.: "Advances in Rotor Performance and Turbulent Wake Simulation using DES and Adaptive Mesh Refinement", 7th International Conference on Computational Fluid Dynamics, Paper ICCFD7-3506, Big Island, HI, USA, Jul 9–13, 2012.

[3] Öhrle, C., Schäferlein, U., Keßler, M., Krämer, E.: "Higher-order Simulations of a Compound Helicopter using Adaptive Mesh Refinement", 74th Annual Forum of the American Helicopter Society, Phoenix, AZ, USA, May 14–17, 2018.

[4] Hariharan, N., Egolf, A., Sankar, L.: "Simulation of Rotor in Hover: Current State and Challanges", 52nd AIAA Aerospace Sciences Meeting, National Harbor, MD, USA, Jan 13–17, 2014. doi: 10.2514/6.2014-0041.

[5] Potsdam, M.: "UH-60A Rotor Tip Vortex Prediction and Comparison to Full-Scale Wind Tunnel Measurements", 70th Annual Forum of the American Helicopter Society, Montréal, Canada, May 20–22, 2014.

[6] Chaderjian, N. M., Buning, P. G.: "High Resolution Navier–Stokes Simulation of Rotor Wakes", American Helicopter Society 67th Annual Forum, Virginia Beach, VA, USA, May 3–5, 2011.

[7] Bernal, L. P., Roshko, A.: "Streamwise Vortex Structure in Plane Mixing Layers", *Journal of Fluid Mechanics* **170**, 1986, pp. 499–525. doi: 10.1017/S002211208600099X.

[8] Gibeau, B., Koch, C. R., Ghaemi, S.: "Secondary Instabilities in the Wake of an Elongated Two–Dimensional Body with a Blunt Trailing Edge",

Journal of Fluid Mechanics **846**, 2018, pp. 578–604.
doi: 10.1017/jfm.2018.285.

[9] Martin, P. B., Leishman, J. G.: "Trailing Vortex Measurements in the Wake of a Hovering Rotor Blade with Various Tip Shapes", 58th Annual Forum of the American Helicopter Society, Montréal, Canada, June 11–13, 2001.

[10] Abras, J. N., Narducci, R., Hariaharan, N.: "Wake Breakdown of High–fidelity Simulations of a Rotor in Hover", AIAA Scitech Forum, San Diego, CA, USA, Jan 7–11 2019.
doi: 10.2514/6.2019-0593.

[11] Egolf, T. A., Hariharan, N., Narducci, R., Reed, E.: "AIAA Standardized Hover Simulation: Hover Performance Prediction Status and Outstanding Issues", 55th AIAA Aerospace Sciences Meeting, Grapevine, TX, USA, Jan 9–13, 2017.
doi: 10.2514/6.2017-1429.

[12] Raffel, M., Bauknecht, A., Ramasamy, M., Yamauchi, G. K., Heineck, J. T., Jenkins, L. N.: "Contributions of Particle Image Velocimetry to Helicopter Aerodynamics", *AIAA Journal* **55**(9), 2017, pp. 2859–2874.
doi: 10.2514/1.J055571.

[13] Felli, M., Dubbioso, G., Falchi, M., "Tomographic–PIV Survey of the Near–Field Hydrodynamic and Hydroacoustic Characteristics of a Marine Propeller", *Journal of Ship Research* **59** (4), 2015, pp. 201–208.
doi: 10.5957/JOSR.59.4.150043.

[14] Schanz, D., Gesemann, S., Schröder, A.: "Shake-The-Box: Lagrangian Particle Tracking at High Particle Image Densities", *Experiments in Fluids* **57** (5), 2016, pp. 70.
doi: 10.1007/s00348-016-2157-1.

[15] Gesemann, S., Huhn, F., Schanz, D., Schröder, A.: "From Noisy Particle Tracks to Velocity, Acceleration and Pressure Fields using B-splines and Penalties", 18th International Symposium on the Application of Laser and Imaging Techniques to Fluid Mechanics, Lisbon, Portugal, July 4–7, 2016.

[16] Bosbach, J., Kühn, M., Wagner, C.: "Large Scale Particle Image Velocimetry with Helium Filled Soap Bubbles", *Experiments in Fluids* **46** (3), 2009, pp. 539–547.
doi: 10.1007/s00348-008-0579-0.

[17] Huhn, F., Schanz, D., Gesemann, S., Dierksheide, U., van de Meerendonk, R., Schröder, A.: "Large–Scale Volumetric Flow Measurement in a Pure Thermal Plume by Dense Tracking of Helium–Filled Soap Bubbles", *Experiments in Fluids* **58** (9), 2017, pp. 116.
doi: 10.1007/s00348-017-2390-2.

[18] Wieneke, B.: "Volume Self–Calibration for 3D Particle Image Velocimetry", *Experiments in Fluids* **45** (4), 2008, pp. 549–556.
doi: 10.1007/s00348-008-0521-5.

[19] Schanz, D., Gesemann, S., Schröder, A., Wieneke, B., Novara, M.: "Non–Uniform Optical Transfer Functions in Particle Imaging: Calibration and Application to Tomographic Reconstruction", *Measurement Science and Technology* **24**, 2013.
doi: 10.1088/0957-0233/24/2/024009.

[20] Novara, M., Schanz, D., Geisler, R., Gesemann, S., Voss, C., Schröder, A.: "Multi–Exposed Recordings for 3D Lagrangian Particle Tracking with Multi–Pulse Shake–The–Box", *Experiments in Fluids* **60** (3), 2019, pp. 44.
doi: 10.1007/s00348-019-2692-7.

[21] Caridi, G. C. A., Sciacchitano, A., Scarano, F.: "Helium–Filled Soap Bubbles for Vortex Core Velocimetry", *Experiments in Fluids* **58** (9), 2017, pp. 130.
doi: 10.1007/s00348-017-2415-x.

[22] Gao, Y., Liu, C.: "Rortex and Comparison with Eigenvalue–Based Vortex Identification Criteria", *Physics of Fluids* **30** (8), 2018.
doi: 10.1063/1.5023001.

[23] Van der Wall, B., Richard, H.: "Analysis Methodology for 3C-PIV Data of Rotary Wing Vortices", *Experiments in Fluids* **40** (5), 2006, pp. 798–812.
doi: 10.1007/s00348-006-0117-x.

[24] Bauknecht, A., Ewers, B., Schneider, O., Raffel, M.: "Blade Tip Vortex Measurements on Actively Twisted Rotor Blades", *Experiments in Fluids* **58** (5), 2017, pp. 49.
doi: 10.1007/s00348-017-2312-3.

[25] Light, J. S.: "Tip Vortex Geometry of a Hovering Helicopter Rotor in Ground Effect", *Journal of the American Helicopter Society* **38** (2), 1993, pp. 34–42.
doi: 10.4050/JAHS.38.34.

[26] Schwarz, C., Bauknecht, A., Mailänder, S., Raffel, M.: "Wake Characterization of a Free–Flying Model Helicopter in Ground Effect", *Journal of the American Helicopter Society* **64** (1), 2019, pp. 1–16.
doi: 10.4050/JAHS.64.012010.

[27] Kutz, B. M., Keßler, M., Krämer, E.: "Experimental and Numerical Examination of a Helicopter Hovering in Ground Effect", *CEAS Aeronautical Journal* **4** (4), 2013, pp. 397–408.
doi: 10.1007/s13272-013-0084-x.

[28] Schwarz, C., Bauknecht, A., Wolf, C. C., Coyle, A., Raffel, M.: "A Full–Scale Rotor–Wake Investigation of a Free–Flying Helicopter in Ground Effect Using BOS and PIV", 75th Annual Forum of the Vertical Flight Society, Philadelphia, PA, USA, May 13–16, 2019.

[29] Quaranta, H. U., Bolnot, H., Leweke, T.: "Long–Wave Instability of a Helical Vortex", *Journal of Fluid Mechanics* **780**, 2015, pp. 687–716. doi: 10.1017/jfm.2015.479.
[30] Ohanian, C. V., McCauley, G. J., Savaş, Ö., "A Visual Study of Vortex Instabilities in the Wake of a Rotor in Hover", *Journal of the American Helicopter Society* **57** (4), 2012, pp. 1–8. doi: 10.4050/JAHS.57.042005.
[31] Leweke, T., Le Dizès, S., Williamson, C. H. K., "Dynamics and Instabilities of Vortex Pairs", *Annual Review of Fluid Mechanics* **48**, 2016, pp. 507–541. doi: 10.1146/annurev-fluid-122414-034558.
[32] Kindler, K., Mulleners, K., Richard, H., van der Wall, B. G., Raffel, M.: "Aperiodicity in the Near–Field of Full–Scale Rotor Blade Tip Vortices", *Experiments in Fluids* **50** (6), 2011, pp. 1601–1610. doi: 10.1007/s00348-010-1016-8.